Journal of Materials Chemistry C

ROYAL SOCIETY OF CHEMISTRY

PAPER

View Article Online
View Journal | View Issue

Cite this: J. Mater. Chem. C, 2024, 12, 1958

Impact of substituent position on crystal structure and photoconductivity in 1D and 2D lead(II) benzenethiolate coordination polymers†

Ryohei Akiyoshi, *[a] Akinori Saeki, [b] Kazuyoshi Ogasawara [a] and Daisuke Tanaka *[a]

Received 26th November 2023,
Accepted 25th December 2023

DOI: 10.1039/d3tc04362b

rsc.li/materials-c

Coordination polymers containing a sulfur coordination atom (S-CPs) are an emerging class of materials with unique optoelectronic properties resulting from their inorganic metal–sulfur $(-M-S-)_n$ networks. Although the structural dimensionalities of $(-M-S-)_n$ networks govern the semiconductive properties of S-CPs, few systematic investigations have examined the impact of these dimensionalities on their semiconductive nature. In this study, we explored the relationship between the $(-Pb-S-)_n$ dimensionality and photoconductivity. We systematically synthesized Pb(II) S-CPs with the formula [Pb(*x*-SPhOMe)$_2$] (*x* = *ortho* (**KGF-32**), *meta* (**KGF-33**), and *para* (**KGF-34**); HSPhOMe = methoxybenzenthiol). Single-crystal X-ray diffraction showed that **KGF-32** and **KGF-34** featured holodirected coordination spheres, but 1D $(-Pb-S-)_n$ chains with $[PbO_2S_4]$ octahedra and 2D $(-Pb-S-)_n$ layers with $[PbS_6]$ octahedra, respectively. In contrast, **KGF-33** features a 1D $(-Pb-S-)_n$ chain comprising a hemidirected $[PbS_5]$ coordination sphere. Notably, time-resolved microwave conductivity measurements and first-principles calculations revealed that the 2D-extended $(-Pb-S-)_n$ layer with the holodirected $[PbS_6]$ octahedron observed in **KGF-34** served as a pathway for electron mobility. The findings of this study provide further design strategies for fabricating highly photoconductive Pb(II) S-CPs.

Introduction

Coordination polymers containing a sulfur coordination atom (S-CPs)[1–5] have attracted increasing attention because of their potential applications in photocatalysts,[6–8] gas sensors,[9–11] and electronic devices.[12–14] The inorganic $(-M-S-)_n$ structures of the S-CPs induce unique optoelectronic properties such as visible-light absorption and high charge mobility.[15,16] As the structural dimensionalities of the $(-M-S-)_n$ networks significantly affect the band gap energies and charge mobilities of S-CPs,[17] the engineering of the $(-M-S-)_n$ network structure based on the precise design of organic ligand moieties is crucially important for fine-tuning semiconductive properties. However, to date, there have been few systematic investigations into the tuning of the $(-M-S-)_n$ dimensionalities of S-CPs.

Benzenethiol derivatives (HSPhX, X = substituents) are promising organic ligands for the construction of S-CPs with a $(-M-S-)_n$ network. The HSPh-derived ligands have facile potential for modification, thus yielding 1D,[18–20] 2D,[12,21,22] and 3D $(-M-S-)_n$ networks[23–25] that serve as pathways for charge delocalization.[5] For example, S-CPs containing 3d transition metal ions (*i.e.* Mn^{2+}, Fe^{2+}, and Co^{2+}) often exhibit 1D architectures with 1D $(-M-S-)_n$ chains.[26–28] Conversely, S-CPs with d^{10} coinage metal ions (*i.e.*, Cu^+, Ag^+, and Au^+) undergo a $(-M-S-)_n$ dimensionality change depending on substituent species.[12,18,29] A recent report also showed that the electron-donating ability of the substituent employed on the HSPh skeleton in the Pb(II) S-CPs affects the $(-M-S-)_n$ dimensionality.[30] Although the effect of substituent species on the obtained $(-M-S-)_n$ networks has been well investigated in the aforementioned study, the correlation between $(-M-S-)_n$ dimensionalities and semiconductive properties such as photoconductivity has remained unclear. To further elucidate the aforementioned correlation, a systematic synthesis of S-CPs with the same composition but different $(-M-S-)_n$ dimensionalities is required.

[a] Department of Chemistry, School of Science, Kwansei Gakuin University, 1 Gakuen Uegahara, Sanda, Hyogo 669-1330, Japan. E-mail: r.akiyoshi@kwansei.ac.jp, dtanaka@kwansei.ac.jp

[b] Department of Applied Chemistry, Graduate School of Engineering, Osaka University, 2-1 Yamadaoka, Suita, Osaka 565-0871, Japan

† Electronic supplementary information (ESI) available: SEM textures, crystallographic data, asymmetric units, bond length, coordination mode of SPhOMe anions, structure focusing on $(-Pb-S-)_n$ network, packing structure, dinuclear unit of **KGF-33**, 2D layer stacking of **KGF-34**, simulated and experimental PXRD patterns, TGA results, PXRD patters after immersing in various solvents, PYS results, TRMC results of **KGF-32** and **KGF-33**, TRMC results of photoconductive S-CPs, distribution of the VBM and CBM. CCDC 2308865–2308867. For ESI and crystallographic data in CIF or other electronic format see DOI: https://doi.org/10.1039/d3tc04362b

In the present study, we focused on the Pb(II) ion because Pb(II) S-CPs reported by our group serve as excellent semiconductive materials that are utilized as photocatalysts.[6,7] Furthermore, Pb(II) S-CPs exhibit either a holodirected coordination sphere whose Pb–S bonds are distributed throughout the surface of an encompassing globe or a hemidirected coordination sphere whose Pb–S bonds are directed throughout only part of an encompassing globe depending on ligand design.[31] As the holodirected coordination sphere forms more covalent bonds than those of the hemidirected coordination sphere, the local structure around Pb(II) centers as well as the $(–Pb–S–)_n$ dimensionality are expected to influence the semiconductive properties in the Pb(II) S-CPs. However, the impact of the local coordination structure and $(–Pb–S–)_n$ dimensionality on the photoconductivity of Pb(II) S-CPs remains largely unexplored. Herein, we investigated the influence of the local structure around Pb(II) ions and $(–Pb–S–)_n$ network structures on semiconductive properties by systematically synthesizing Pb(II) S-CPs with methoxybenzenethiol (HSPhOMe) ligands (Fig. 1). By changing the position of the methoxy substituent on the HSPh skeleton, we synthesized three Pb(II) S-CPs with a formula of $[Pb(x\text{-SPhOMe})_2]_n$ (x = *ortho* (**KGF-32**), *meta* (**KGF-33**), and *para* (**KGF-34**); HSPhOMe = methoxybenzenthiol) and analyzed their photoconductivity using time-resolved microwave conductivity (TRMC) and first-principles calculations.

Results and discussion

Single crystal X-ray diffraction (SCXRD) analyses

The syntheses were performed in an autoclave using the solvothermal method (see the Experimental section). Single crystals of **KGF-32**, **KGF-33**, and **KGF-34** were obtained as pale-yellow needle crystals, light-yellow needle crystals, and dark brown plate crystals, respectively (Fig. 1 and Fig. S1, ESI†). The crystal structures were determined using single-crystal X-ray diffraction (SCXRD) at 150 K. The crystal parameters are presented in Table S1 (ESI†), with the full structural data available from the CCDC (CCDC 2308865–2308867†). **KGF-32** crystallizes in the monoclinic $P2_1/c$ space group. The asymmetric unit consists of one Pb(II) ion and two chelating *o*-SPhOMe$^-$ anions (Fig. S2a, ESI†). The Pb(II) center was coordinated by two O atoms of the methoxy group and four S atoms of the thiolate, yielding a holodirected coordination geometry with a distorted $[PbO_2S_4]$ octahedron (Fig. 2a). The Pb–O bond lengths are 2.703 and 2.862 Å, whereas the Pb–S bond distance falls in the range 2.689–3.384 Å (Fig. S3a, ESI†). The S atoms of thiolate act as a μ_2-S atom (Fig. S4a, ESI†), which connects the neighboring $[PbO_2S_4]$ octahedra by edge sharing, consequently forming a 1D structure along the *c*-axis (Fig. 2b). Thus, **KGF-32** has a 1D structure containing a 1D $(–Pb–S–)_n$ chain with holodirected $[PbO_2S_4]$ octahedra (Fig. S5a, ESI†). Furthermore, 1D chains were arranged by weak van der Waals (vdW) interactions between the 1D chains (Fig. S6a, ESI†).

Similar to **KGF-32**, **KGF-33** crystallized in the monoclinic $P2_1/c$ space group, and the formation of a 1D-extended structure was evident. However, in contrast to **KGF-32** which features a holodirected coordination sphere with a $[PbO_2S_4]$ octahedron, **KGF-33** features a hemidirected coordination mode with a $[PbS_5]$ square pyramidal coordination geometry and five S atoms of *m*-SPhOMe bound to the Pb(II) ion (Fig. 2c). The Pb–S bond lengths were in the range 2.693–3.204 Å (Fig. S3b, ESI†). The S

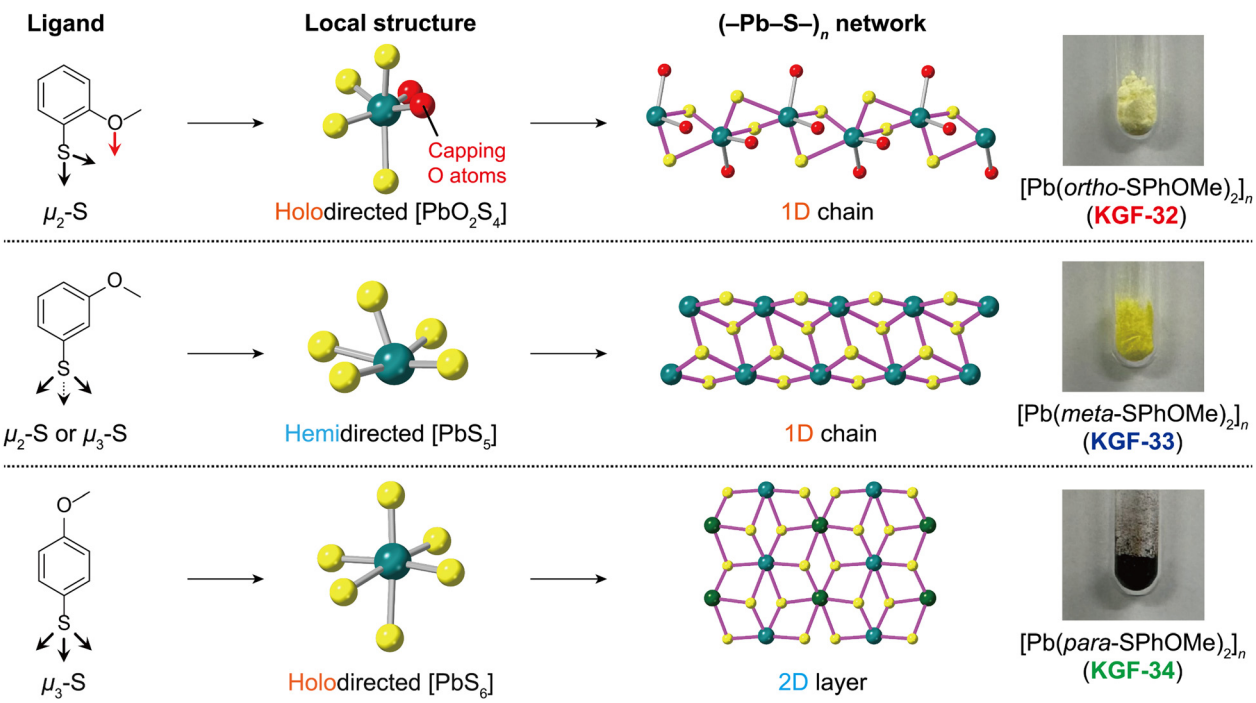

Fig. 1 Schematic illustration of structures for $[Pb(x\text{-SPhOMe})_2]_n$ (x = *ortho* (**KGF-32**), *meta* (**KGF-33**), and *para* (**KGF-34**)). From left to right: Coordination modes of SPhOMe ligands, local structures around Pb(II) ions, $(–Pb–S–)_n$ dimensionality, photographs of corresponding samples.

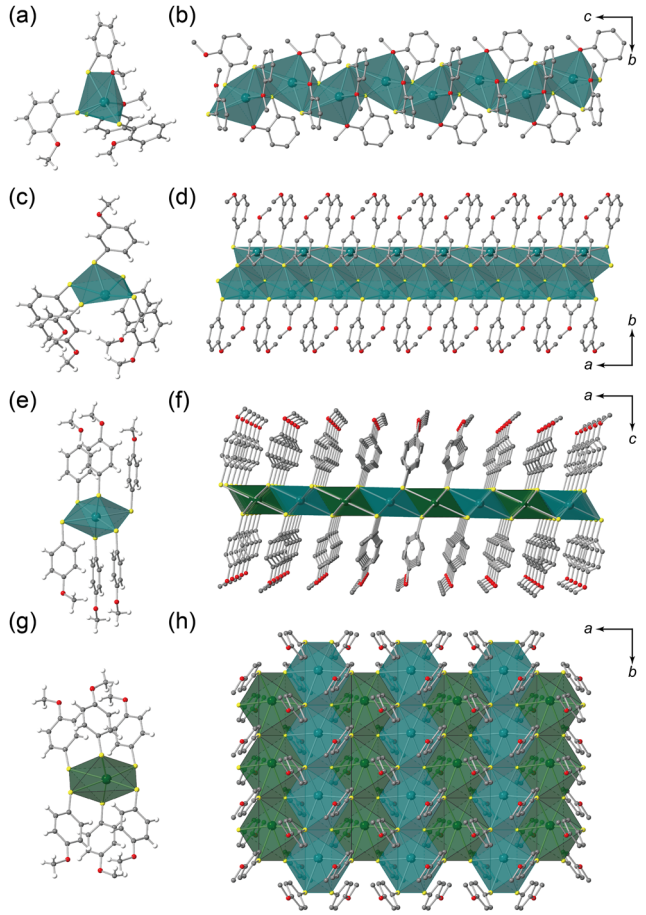

Fig. 2 Crystal structures of **KGF-32**, **KGF-33**, and **KGF-34**. (a) Holodirected sphere with a [PbO_2S_4] octahedron; (b) 1D chain structure of **KGF-32**; (c) Hemidirected sphere with a [PbS_5] square pyramid; (d) 1D chain structure of **KGF-33**; (e) and (g) Holodirected [PbS_6] octahedron; (f) and (h) 2D layer structure of **KGF-34**. Color code: Pb: green, S: yellow, C: grey, O: red, H: white.

atoms exhibit two coordination modes: S1 is a μ_2-S atom, whereas S2 is a μ_3-S atom (Fig. S4b, ESI†). The μ_2-S1 atom behaves as a bridging atom to form a dinuclear coordination unit (Fig. S7, ESI†). In contrast, the μ_3-S2 atom serves to bridge the dinuclear units, forming a 1D chain structure along the *a*-axis (Fig. 2d, Fig. S5b, ESI†). Consequently, **KGF-33** features a 1D chain structure composed of a 1D $(–Pb–S–)_n$ chain in the hemidirected [PbS_5] coordination mode. The resultant 1D chains were further assembled by weak vdW interactions (Fig. S6b, ESI†).

KGF-34 was prepared using *p*-HSPhOMe crystallized in the monoclinic space group $P2/n$, consistent with recently reported literature.[30] It contained two crystallographically non-equivalent Pb(II) ions (Fig. S2c, ESI†), whose Pb(II) centers had a holodirected coordination structure with a [PbS_6] octahedron (Fig. 2e and g). The Pb–S bond length was 2.835–3.321 Å (Fig. S3c, ESI†). All S atoms serve as μ_3-S to form a 2D layer structure parallel to the *ab*-plane (Fig. S4c, ESI†). Notably, the 2D layer of **KGF-34** contains a 2D-extended $(–Pb–S–)_n$ layer comprising holodirected [PbS_6] octahedra (Fig. 2f and h, Fig. S5c, ESI†). The resultant 2D layer was stacked by weak vdW interactions with an interlayer distance of 17.210 Å (Fig. S6c and S8, ESI†).

According to previously reported literature,[30,31] the electron density of thiol groups has a significant impact on both the local structure around the Pb(II) ions and the coordination numbers, which in turn undergo a $(–Pb–S–)_n$ dimensionality change. Specifically, the increased electron density of the thiol group contributes to the transition from the hemidirected to the holodirected mode and increases the coordination number of the Pb–S unit, consequently resulting in the formation of a 2D $(–Pb–S–)_n$ layer. In the current study, a structural change in the coordination sphere, depending on the position of the methoxy substituents, was evident. As anticipated, **KGF-33** with an electron-donating methoxy substituent at *meta*-position featured a hemidirected [PbS_5] structure, whereas **KGF-32** and **KGF-34** with methoxy substituents at *ortho*- and *para*-positions exhibited holodirected structures with [PbO_2S_4] and [PbS_6] units, respectively. These structural variations in the coordination sphere also influence the dimensionality of the $(–Pb–S–)_n$ structure. **KGF-33** exhibited a 1D $(–Pb–S–)_n$ chain structure attributed to its hemidirectional structure, whereas **KGF-34** displayed a 2D $(–Pb–S–)_n$ layer due to its holodirectional structure. These results are consistent with the previously reported trends. Notably, **KGF-32** with a methoxy substituent at the *ortho*-position featured a 1D $(–Pb–S–)_n$ chain despite its holodirected structure. This may be attributed to the presence of O coordination atoms that disturb the 2D extension of the $(–Pb–S–)_n$ network through μ_3-S atoms, thereby leading to the formation of a 1D chain structure. The purities of the respective products were confirmed by powder X-ray diffraction (PXRD) and elemental analyses before the physical measurements (Fig. S9, ESI†).

Thermal and chemical stability

The thermal stabilities of **KGF-32**, **KGF-33**, and **KGF-34** were investigated by thermogravimetry analyses (TGA). Fig. S10 (ESI†) displays TG plots in the temperature range 30–600 °C under N_2 atmosphere, wherein no weight loss was observed up to approximately 187 °C for **KGF-32**, 136 °C for **KGF-33**, and 205 °C for **KGF-34**. The enhanced thermal stabilities of **KGF-32** and **KGF-34** may be attributed to the holodirectional structures with a more covalent Pb–S bond. The chemical stability in water, 1 M HCl aq., 1 M NaOH aq., and organic solvents was also examined by obtaining the PXRD pattern for the sample, which had been immersed in the corresponding solvent for 24 h. As depicted in Fig. S11 (ESI†), all S-CPs exhibited remarkable stability in water. However, **KGF-32** and **KGF-34**, which have holodirected coordination spheres, were unstable under acidic conditions but remained stable under basic conditions. Conversely, **KGF-33**, featuring a hemidirected coordination sphere, exhibited instability under both acidic and basic conditions. The resistance to basic conditions observed in **KGF-32** and **KGF-34** may be attributed to the holodirected coordination spheres with a more covalent Pb–S bond. The series of Pb(II)-based S-CPs also exhibited remarkable stability in organic solvents (Fig. S12, ESI†). Accordingly, the resultant thermal and chemical stabilities may be attributed to the strong bonds between the Pb(II) ions and the S coordination atoms.

Semiconductive properties

The electronic and optical properties were evaluated using diffuse-reflectance ultraviolet-visible-near-infrared (DR-UV-Vis-NIR) spectroscopy. **KGF-32** and **KGF-33** display broad absorption below 500 nm, whereas **KGF-34** shows visible light absorption with an absorption edge at 765 nm (Fig. 3a). By extrapolating a Tauc plot in the forms of $[F(R) \times h\nu]^{1/2}$ *vs.* $h\nu$ for the indirect semiconductors (**KGF-33** and **KGF-34**) and $[F(R) \times h\nu]^{2}$ *vs.* $h\nu$ for the direct semiconductor (**KGF-32**) (see the following first-principles calculation results), the optical bandgaps of **KGF-32**, **KGF-33**, and **KGF-34** were estimated to be 2.93, 2.51, and 1.64 eV, respectively (Fig. 3b). Photoelectron yield spectroscopy (PYS) was employed for determining the absolute valence band maximum (VBM) level,[32] in which the VBM levels were determined to be −5.66, −5.63, and −5.18 eV below the vacuum level for **KGF-32**, **KGF-33**, and **KGF-34**, respectively (Fig. S13, ESI†). Considering the optical bandgap obtained from the DR-UV-Vis-NIR results, the absolute conduction band minimum (CBM) levels of **KGF-32**, **KGF-33**, and **KGF-34** were determined to be −2.73, −3.12, and −3.54 eV below the vacuum level, respectively (Fig. 3c).

The photoconductive properties of **KGF-32**, **KGF-33**, and **KGF-34** were investigated using TRMC experiments. TRMC is a contactless technique that uses high-frequency microwaves to probe the laser-induced transient increase in conductivity, providing information on charge transport on a multi-nanometer length scale.[33,34] The $\varphi\sum\mu_{max}$ values (φ = quantum yield of charge-carrier generation; $\sum\mu$ = sum of the hole and electron mobilities) were determined to be 2.5×10^{-5} cm^2 V^{-1} s^{-1} for **KGF-32**, 3.8×10^{-5} cm^2 V^{-1} s^{-1} for **KGF-33**, and 1.4×10^{-3} cm^2 V^{-1} s^{-1} for **KGF-34** (Fig. 3d and Fig. S14, ESI†). The $\varphi\sum\mu_{max}$ value of **KGF-34** is two orders of magnitude higher than those of **KGF-32** and **KGF-33**. Notably, the $\varphi\sum\mu_{max}$ value obtained for **KGF-34** is the highest among the previously reported photoconductive CPs and MOFs (Table S2, ESI†). This remarkable photoconductivity reflects the coordination environment around the Pb(II) ion and $(-Pb-S-)_n$ dimensionality, as discussed below.

First-principles calculations

In the Pb(II) S-CPs, the local structure around the Pb(II) centers and the $(-Pb-S-)_n$ dimensionality are expected to affect the electronic structures because the bond of the holodirected structure is more covalent than that observed in the hemidirected structure. Therefore, we evaluated the band structure using first-principles calculations to elucidate the relationship between crystal structure and photoconductivity (details of the calculation method are presented in the Experimental section).[35] The calculations demonstrated that **KGF-32** is an indirect transition semiconductor, whereas **KGF-33** and **KGF-34** are direct transition semiconductors. The calculated bandgaps, determined by the energy difference between the VBM and the CBM, are 2.84 eV for **KGF-32**, 2.58 eV for **KGF-33**, and 1.18 eV for **KGF-34**. These values are in good agreement with the trends obtained from DR-UV-Vis-NIR spectroscopy. Notably, the calculated band gaps were typically lower than the experimental values.[36] In the simulated band structures, **KGF-32** and **KGF-33**

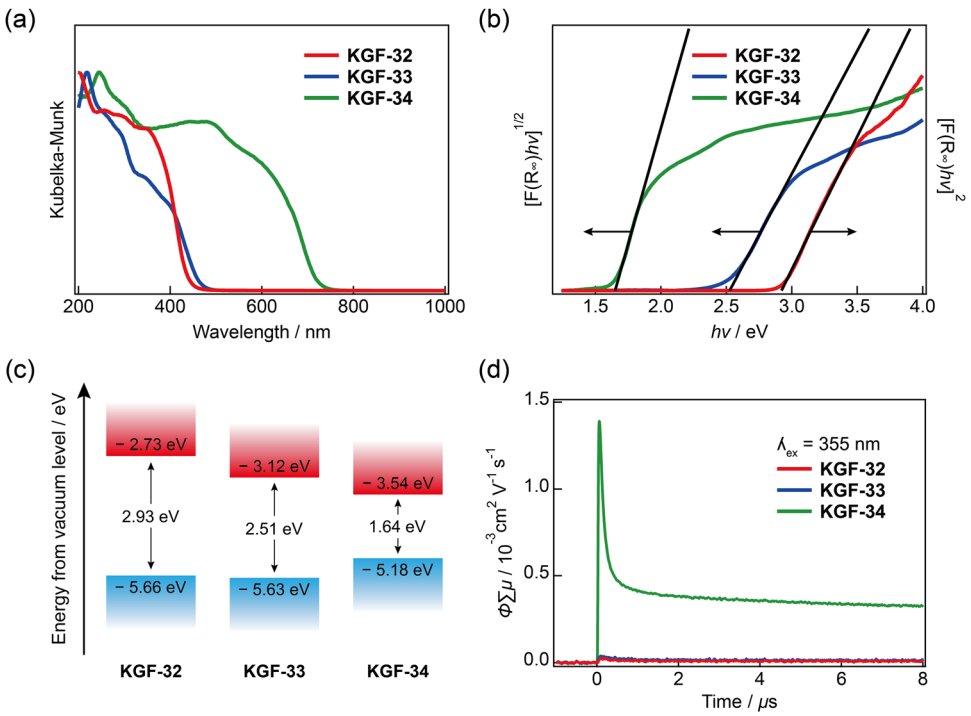

Fig. 3 Semiconductive natures of **KGF-32**, **KGF-33**, and **KGF-34**. (a) DR-UV-Vis-NIR spectra; (b) Tauc plot; (c) Electronic energy diagram below vacuum level. The VBM energy level was determined by PYS experiments, as depicted in Fig. S13 (ESI†); and (d) Results of TRMC experiments (λ_{ex} = 355 nm; red: **KGF-32**, blue: **KGF-33**, green: **KGF-34**).

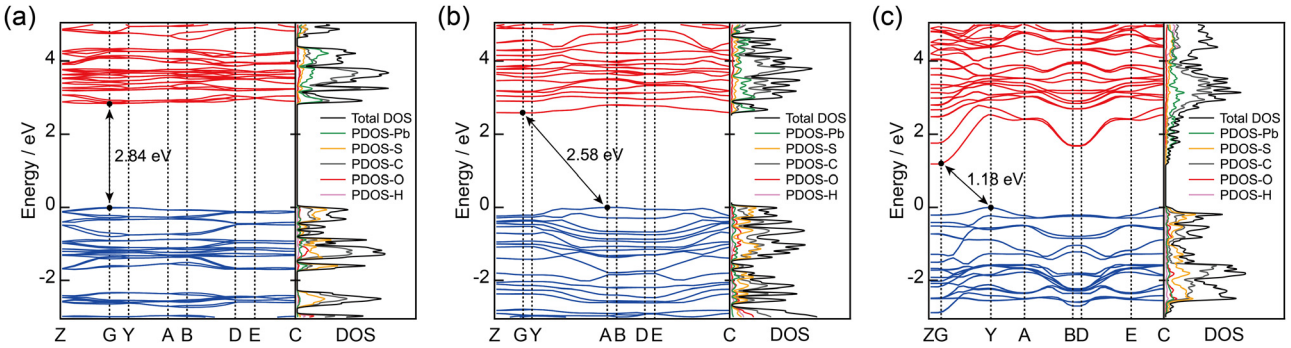

Fig. 4 Band structures and DOS profiles of (a) **KGF-32**, (b) **KGF-33**, and (c) **KGF-34**. VBM energy level is presented as zero.

each had flat bands with a dispersion width <0.3 eV in both the VBM and CBM (Fig. 4a and b). **KGF-34** also showed a relatively flat band in the VBM while exhibiting an anomalous CBM dispersion with a dispersion width of approximately 1.6 eV (Fig. 4c). The direction of the CBM dispersion obtained for **KGF-34** corresponded to the in-plane direction of the 2D layer (G–Y, A–B, and D–E). Because typical semiconductive CPs possess a flat band structure with <0.3 eV dispersion widths, the resultant steep CBM dispersion of **KGF-34** strongly indicates that the electron mobility of **KGF-34** along the 2D layer structure is remarkable. The band dispersion trends observed for **KGF-32**, **KGF-33**, and **KGF-34** are fully consistent with the TRMC results.

Density of states (DOS) analyses provided additional insight into the origin of the bands from the elements, where the black line represents the total DOS, and the other colored lines represent the partial DOS (PDOS). In the PDOS analyses of **KGF-32** and **KGF-33**, the C and S atoms largely contributed to the VBM. The CBM of **KGF-32** was dominated by Pb and C atoms, with a negligible contribution from S atoms, whereas the CBM of **KGF-33** mainly consisted of Pb, with small contributions from S and C atoms. For **KGF-34**, the VBM mainly consisted of C and S atoms, whereas the CBM largely consisted of Pb and S atoms. The distribution of the VBM and CBM also supported the PDOS results (Fig. S15–S17, ESI†). In particular, the VBM of **KGF-34** was localized on the SPhOMe ligands, whereas the CBM was delocalized through the 2D $(–Pb–S–)_n$ layer. These results clearly reveal that the 2D $(–Pb–S–)_n$ layer, composed of holodirected $[PbS_6]$ coordination spheres, serves as a pathway for electron mobility.

Overall, the series of Pb(II) S-CPs exhibited photoconductivity that reflected the local structure around the Pb(II) ions and $(–Pb–S–)_n$ dimensionality. As expected, **KGF-33** with methoxy substituents at the *meta*-position displayed poor photoconductivity with a flat band owing to the hemidirected coordination sphere with more ionic bonds. In contrast, **KGF-34** with methoxy substituents at the *para*-position exhibited high photoconductivity with a large CBM dispersion because of its holodirected coordination environment with more covalent bonds. Although **KGF-32** with methoxy substituents at the *ortho*-position featured a holodirected coordination sphere, it exhibited lower photoconductivity than **KGF-33** and **KGF-34**. From this perspective, we suggest that a 2D-arranged, holodirected $[PbS_6]$ octahedron is crucial for constructing a pathway for electron mobility.

Conclusions

We systematically synthesized three Pb(II) S-CPs of $[Pb(SPhOMe)_2]_n$ with various coordination environments and inorganic $(–Pb–S–)_n$ dimensionalities by changing the positions of the methoxy substituents. Because of the electron-donating methoxy group at the *ortho*- and *para*-positions, **KGF-32** and **KGF-34** featured holodirected coordination spheres, 1D $(–Pb–S–)_n$ chains with $[PbO_2S_4]$ octahedra and 2D $(–Pb–S–)_n$ layers with $[PbS_6]$ octahedra, respectively. In contrast, **KGF-33** with a methoxy substituent at the *meta*-position features a 1D $(–Pb–S–)_n$ layer comprising a hemidirected $[PbS_6]$ coordination sphere. Our systematic investigation using TRMC measurements and first-principles calculations revealed that a 2D-extended $(–Pb–S–)_n$ layer composed of holodirected $[PbS_6]$ octahedra is crucial for inducing high electron mobility. These results provide new insights into design strategies for fabricating highly photoconductive Pb(II) S-CPs.

Experimental

Materials

$Pb(NO_3)_2$ ($\geq$99.9%) and methanol (MeOH) ($\geq$99.5%) were purchased from FUJIFILM Wako Pure Chemical Industries, Osaka, Japan. *o*-Methoxybenzenethiol (*o*-HSPhOMe) ($\geq$98.0%), *m*-methoxybenzenethiol (*m*-HSPhOMe) ($\geq$98.0%), and *p*-methoxybenzenethiol (*p*-HSPhOMe) ($\geq$96.0%) were obtained from Tokyo Chemical Industry Co., Ltd., Tokyo, Japan. Acetone ($\geq$99.0%) was obtained from Kanto Chemical Co., Inc. (Japan). All chemicals and solvents employed in the synthesis were of reagent grade and used without further purification.

Synthetic procedures

Synthesis of KGF-32. $Pb(NO_3)_2$ (198.7 mg, 0.6 mmol) and *o*-HSPhOMe (168.2 mg, 1.2 mmol) were dissolved in MeOH/H_2O (8.0 mL, v:v = 1:1) and sealed in a 16 mL Teflon-lined stainless-steel container. The solution was heated to 60 °C for 48 h. Then, the container was cooled to 30 °C for 12 h in the autoclave. The residue was collected by centrifugation

(4000 rpm, 3 min) and washed with MeOH. The resulting solid was dried under vacuum to yield the product as pale-yellow, needle-like crystals. Yield: 94.6 mg (66.6%). Anal. $C_{14}H_{14}O_2PbS_2$: calcd C 34.63, H 2.91, N 0.00; found C 34.62, H 2.87, N 0.00.

Synthesis of KGF-33. $Pb(NO_3)_2$ (198.7 mg, 0.6 mmol) and *m*-HSPhOMe (168.2 mg, 1.2 mmol) were dissolved in acetone/H_2O (8.0 mL, v : v = 1 : 1) and sealed in a 16 mL Teflon-lined stainless-steel container. The solution was heated to 80 °C for 48 h. Subsequently, the container was cooled to 30 °C for 12 h in the autoclave. The residue was collected by centrifugation (4000 rpm, 3 min) and washed with MeOH. The resulting solid was dried under vacuum to yield the product as yellow needle-like crystals. Yield: 116.6 mg (40.0%). Anal. $C_{14}H_{14}O_2PbS_2$: calcd C 34.63, H 2.91, N 0.00; found C 34.54, H 2.87, N 0.00.

Synthesis of KGF-34. $Pb(NO_3)_2$ (198.7 mg, 0.6 mmol) and *p*-HSPhOMe (168.2 mg, 1.2 mmol) were dissolved in acetone/H_2O (8.0 mL, v : v = 1 : 1) and sealed in a 16 mL Teflon-lined stainless-steel container. The solution was heated to 80 °C for 48 h. Then, the container was cooled to 30 °C for 12 h in the autoclave. The residue was collected by centrifugation (4000 rpm, 3 min) and washed with MeOH. The resulting solid was dried under vacuum to yield the product as dark-brown crystalline sheets. Yield: 131.6 mg (45.2%). Anal. $C_{14}H_{14}O_2PbS_2$: calcd C 34.63, H 2.91, N 0.00; found C 34.60, H 2.65, N 0.00.

Methods

Single crystal X-ray diffraction (SCXRD). SCXRD data were collected on a Rigaku Saturn CCD diffractometer equipped with Mo-Kα radiation (λ = 0.71073 Å). The diffraction profiles were integrated using the CrysAlisPro software. The structures were obtained by direct methods using the SHELXT program and refined using SHELXL.[37,38] Anisotropic thermal parameters were used to refine all non-H atoms. All the calculations were performed using the Olex2 crystallographic software package.[39]

Diffuse-reflectance ultraviolet-visible-near-infrared (DR-UV-Vis-NIR) spectroscopy. DR-UV-Vis-NIR spectroscopy was performed using a SHIMADZU UV-3600 UV-Vis-NIR spectrophotometer at wavelengths ranging from 200 nm to 1000 nm. $BaSO_4$ powder was used as the non-adsorbing background. The bandgaps were calculated using the Kubelka–Munk function and the following equation:

$$\frac{K}{S} = F(R) = \frac{(1-R)^2}{2R}$$

where K is the absorption coefficient, S the scattering factor, R the reflectance, and $F(R)$ the KM function. The bandgap was determined from the Tauc plot with $[F(R) \times h\nu]^{1/2}$ *vs.* $h\nu$ (for the indirect semiconductors) and $[F(R) \times h\nu]^2$ *vs.* $h\nu$ (for the direct semiconductor) by extrapolating the linear region to the abscissa.

Photoelectron yield spectroscopy (PYS). Crystalline samples were placed on a conductive carbon tape on a glass substrate, which was connected to the earth wire in a vacuum chamber (10^{-4} Pa) of a Bunko Keiki BIP-KV202GD instrument. The sample was exposed to monochromated ultraviolet (UV) light (4–7 eV corresponding to 355 to 177 nm), and the photoelectrons emitted from the sample were detected. The photon number (power) of UV light was measured by a photodetector prior to the experiment.

Time-resolved microwave conductivity (TRMC) measurement. Crystalline samples on an adhesive tape attached to a quartz substrate were placed in the resonant cavity and exposed to continuous microwave radiation at approximately 9.1 GHz. The third harmonic generation (355 nm) of a Nd:YAG laser (Continuum Inc., Surelite II, pulse duration = 5–8 ns, 10 Hz) was used as the excitation source (incident photon density I_0 = 9.1 × 10^{15} photons cm^{-2} $pulse^{-1}$). The photoconductivity ($\Delta\sigma = A^{-1}\Delta P_r P_r^{-1}$ where A is the sensitivity factor, P_r is the reflected microwave power, and ΔP_r is the change in P_r upon exposure to light) was converted into the product of the quantum yield (φ) and sum of the charge carrier mobilities $\sum\mu$ (= $\mu_+ + \mu_-$) using the relationship $\varphi\sum\mu = \Delta\sigma(eI_0F_{light})^{-1}$, where e and F_{Light} are the electron charge and correction (or filling) factor, respectively. The experiments were performed at 25 °C in air.

First-principles calculation. First-principles calculations were performed using CASTEP 2020 (20.1.0.5). The generalized gradient approximation (GGA) and the Perdew–Burke–Ernzerhof (PBE) exchange correlation potential with the ultrasoft pseudopotential plane-wave method were used. The plane-wave cut-off were set to 570 eV for **KGF-32**, 630 eV for **KGF-33**, and 490 eV for **KGF-34**. The Brillouin zones of **KGF-32**, **KGF-33**, and **KGF-34** were sampled with a 4 × 2 × 4 *k*-point mesh, 3 × 1 × 1 *k*-point mesh, and 13 × 19 × 3 *k*-point mesh, respectively.

Other physical measurements. Elemental analysis was performed using A-Rabbit-Science Japan Co., Ltd, Japan. SEM textures were recorded using a JEOL scanning electron microscope. The acceleration voltage was set at 15 kV. Scanning electron microscopy (SEM) images were acquired using a JEOL JCM-6000 instrument. All samples were sputter-coated with Au prior to analysis. Powder X-ray diffraction (PXRD) was performed on a Rigaku MiniFlex600 diffractometer at 40 kV and 15 mA using a Cu target tube. Samples were examined without grinding, and data were collected in the 2–50° 2θ range using Cu-Kα radiation (λ = 1.54187 Å). Thermogravimetric analysis (TGA) was performed on a Shimadzu DTG-60 instrument. The analysis was conducted in the temperature range of 30–600 °C, with a heating rate of 10 °C min^{-1}, under an N_2 atmosphere.

Author contributions

The manuscript was written with contributions from all authors. All the authors approved the final version of the manuscript.

Conflicts of interest

There are no conflicts to declare.

Acknowledgements

This work was supported by JSPS Grant numbers JP22K14702, JP20H05836, JP20H02577, JP23H01810, and JP23H04637

(Transformative Research Areas (A) ''Supra-ceramics'') and partially supported by the ENEOS Hydrogen Trust Fund. R. A. acknowledges the financial support provided by the Izumi Science and Technology Foundation and the Kawanishi Memorial ShinMaywa Education Foundation. D. T. acknowledges the financial support provided by JST, Grant number JPMJPF2204, and the Samco Foundation. We would like to thank Editage (**https://www.editage.jp**) for the English-language editing.

Notes and references

1 O. Veselska and A. Demessence, *Coord. Chem. Rev.*, 2018, **355**, 240–270.
2 J. Xie, L. Wang and J. S. Anderson, *Chem. Sci.*, 2020, **11**, 8350–8372.
3 Y. Jin, C. Zhang, X. Y. Dong, S. Q. Zang and T. C. W. Mak, *Chem. Soc. Rev.*, 2021, **50**, 2297–2319.
4 Y. Kamakura and D. Tanaka, *Chem. Lett.*, 2021, **50**, 523–533.
5 G. E. Wang, S. Luo, T. Di, Z. Fu and G. Xu, *Angew. Chem., Int. Ed.*, 2022, **61**, e202203151.
6 Y. Kamakura, P. Chinapang, S. Masaoka, A. Saeki, K. Ogasawara, S. R. Nishitani, H. Yoshikawa, T. Katayama, N. Tamai, K. Sugimoto and D. Tanaka, *J. Am. Chem. Soc.*, 2020, **142**, 27–32.
7 Y. Kamakura, S. Yasuda, N. Hosokawa, S. Nishioka, S. Hongo, T. Yokoi, D. Tanaka and K. Maeda, *ACS Catal.*, 2022, **12**, 10172–10178.
8 Y. Kamakura, C. Suppaso, I. Yamamoto, R. Mizuochi, Y. Asai, T. Motohashi, D. Tanaka and K. Maeda, *Angew. Chem., Int. Ed.*, 2023, **62**, e202305923.
9 Y. Li, J. Shu, Q. Huang, K. Chiranjeevulu, P. N. Kumar, G. E. Wang, W. H. Deng, D. Tang and G. Xu, *Chem. Commun.*, 2019, **55**, 10444–10447.
10 H. Jiang, L. Cao, Y. Li, W. Li, X. Ye, W. Deng, X. Jiang, G. Wang and G. Xu, *Chem. Commun.*, 2020, **56**, 5366–5369.
11 Y. Wen, G. E. Wang, X. Jiang, X. Ye, W. Li and G. Xu, *Angew. Chem., Int. Ed.*, 2021, **60**, 19710–19714.
12 A. Pathak, J. W. Shen, M. Usman, L. F. Wei, S. Mendiratta, Y. S. Chang, B. Sainbileg, C. M. Ngue, R. S. Chen, M. Hayashi, T. T. Luo, F. R. Chen, K. H. Chen, T. W. Tseng, L. C. Chen and K. L. Lu, *Nat. Commun.*, 2019, **10**, 1721.
13 G. Xing, Y. Li, Z. Feng, D. J. Singh and F. Pauly, *ACS Appl. Mater. Interfaces*, 2020, **12**, 53841–53851.
14 C. Andrade, S. Hawila, A. Abdallah, J.-L. Rukemampunzi, A. Mesbah, N. Guillou, F. Perret, S. Wuttke, T. Niehaus, R. Debord, O. Boisron, S. Pailhès and A. Demessence, *J. Mater. Chem. C*, 2023, **11**, 14540–14544.
15 L. Sun, T. Miyakai, S. Seki and M. Dinca, *J. Am. Chem. Soc.*, 2013, **135**, 8185–8188.
16 L. Sun, C. H. Hendon, M. A. Minier, A. Walsh and M. Dinca, *J. Am. Chem. Soc.*, 2015, **137**, 6164–6167.
17 T. Wakiya, Y. Kamakura, H. Shibahara, K. Ogasawara, A. Saeki, R. Nishikubo, A. Inokuchi, H. Yoshikawa and D. Tanaka, *Angew. Chem., Int. Ed.*, 2021, **60**, 23217–23224.
18 C. M. Che, C. H. Li, S. S. Chui, V. A. Roy and K. H. Low, *Chem. – Eur. J.*, 2008, **14**, 2965–2975.
19 C. Lavenn, L. Okhrimenko, N. Guillou, M. Monge, G. Ledoux, C. Dujardin, R. Chiriac, A. Fateeva and A. Demessence, *J. Mater. Chem. C*, 2015, **3**, 4115–4125.
20 J. Troyano, Ó. Castillo, P. Amo-Ochoa, J. I. Martínez, F. Zamora and S. Delgado, *CrystEngComm*, 2019, **21**, 3232–3239.
21 C. Lavenn, N. Guillou, M. Monge, D. Podbevsek, G. Ledoux, A. Fateeva and A. Demessence, *Chem. Commun.*, 2016, **52**, 9063–9066.
22 Y. Li, X. Jiang, Z. Fu, Q. Huang, G. E. Wang, W. H. Deng, C. Wang, Z. Li, W. Yin, B. Chen and G. Xu, *Nat. Commun.*, 2020, **11**, 261.
23 I. G. Dance, *J. Am. Chem. Soc.*, 1980, **102**, 3445–3451.
24 I. G. Dance, R. G. Garbutt, D. C. Craig and M. L. Scudder, *Inorg. Chem.*, 1987, **26**, 4057–4064.
25 C. Xu, H.-T. Shi, Z.-F. Xin, A.-Q. Jia and Q.-F. Zhang, *J. Cluster Sci.*, 2014, **25**, 1353–1361.
26 A. Eichhofer and G. Buth, *Dalton Trans.*, 2016, **45**, 17382–17391.
27 A. Eichhofer and S. Lebedkin, *Inorg. Chem.*, 2018, **57**, 602–608.
28 A. Eichhöfer and G. Buth, *Eur. J. Inorg. Chem.*, 2019, 639–646.
29 L. Okhrimenko, C. Cibaka Ndaya, A. Fateeva, G. Ledoux and A. Demessence, *New J. Chem.*, 2020, **44**, 17970–17975.
30 H. Yang, S. Mandal, Y. H. Lee, J. Y. Park, H. Zhao, C. Yuan, L. Huang, M. Chen and L. Dou, *J. Am. Chem. Soc.*, 2023, **145**, 23963–23971.
31 L. Shimoni-Livny, J. P. Glusker and C. W. Bock, *Inorg. Chem.*, 1998, **37**, 1853–1867.
32 R. Nishikubo, N. Ishida, Y. Katsuki, A. Wakamiya and A. Saeki, *J. Phys. Chem. C*, 2017, **121**, 19650–19656.
33 A. Saeki, Y. Koizumi, T. Aida and S. Seki, *Acc. Chem. Res.*, 2012, **45**, 1193–1202.
34 A. Saeki, *Polym. J.*, 2020, **52**, 1307–1321.
35 S. J. Clark, M. D. Segall, C. J. Pickard, P. J. Hasnip, M. I. J. Probert, K. Refson and M. C. Payne, *Z. Kristallogr. - Cryst. Mater.*, 2005, **220**, 567–570.
36 C. Lee, W. Yang and R. G. Parr, *Phys. Rev. B: Condens. Matter Mater. Phys.*, 1988, **37**, 785–789.
37 G. M. Sheldrick, *Acta Crystallogr.*, 2008, **A64**, 112–122.
38 G. M. Sheldrick, *Acta Crystallogr.*, 2015, **C71**, 3–8.
39 O. V. Dolomanov, L. J. Bourhis, R. J. Gildea, J. A. K. Howard and H. Puschmann, *J. Appl. Crystallogr.*, 2009, **42**, 339–341.

